





The Distribution and Accessibility of Geologic Targets near the Lunar South Pole and Candidate Artemis Landing Sites

Sarah. J. Boazman¹ , Jahnvi Shah^{2,3}, Harish⁴, Aleksandra J. Gawronska⁵, Samuel H. Halim⁶, Animireddi V. Satyakumar⁷ , Cosette M. Gilmour⁸, Valentin T. Bickel^{9,10}, Natasha Barrett¹¹, and David A. Kring^{12,13}

¹ ESTEC, European Space Agency, Noordwijk, 2201 AZ, ESA Research Fellow, The Netherlands; Sarah.Boazman@esa.int

² Department of Earth Sciences, University of Western Ontario, London, Ontario, N6A 3K7, Canada

³ Institute for Earth and Space Exploration, University of Western Ontario, London, Ontario, N6A 3K7, Canada

⁴ Space and Planetary Science Center, Khalifa University, UAE

⁵ Department of Geology and Environmental Earth Science, Miami University, Oxford, OH 45056, USA

⁶ Department of Earth and Planetary Sciences, Birkbeck, University of London, London, WC1E 7HX, UK

⁷ Gravity and Magnetic Studies Group, CSIR-National Geophysical Research Institute (CSIR-NGRI), Hyderabad, India

⁸ Centre for Research in Earth and Space Science, York University, Toronto, ON, M3J 1P3, Canada

⁹ ETH Zurich, Zurich, Switzerland

¹⁰ Center for Space and Habitability, University of Bern, Bern, Switzerland

¹¹ Department of Geosciences and Natural Resource Management, University of Copenhagen, DK-1350 Copenhagen K, Denmark

¹² Lunar and Planetary Institute, Universities Space Research Association, Houston, TX, USA

¹³ NASA Solar System Exploration Research Virtual Institute, Mountain View, CA, USA

Received 2022 September 13; revised 2022 November 18; accepted 2022 November 22; published 2022 December 22

Abstract

Transformative lunar science will be driven by the accessibility, recovery, and return to Earth of geological specimens. Isolated boulders, rock exposures, and rocky craters at the lunar south pole all provide opportunities for geologic characterization and sampling of the lunar crust. Here, we present the results of orbital geological mapping of the region surrounding the south pole using Lunar Reconnaissance Orbiter Narrow Angle Camera images (0.5–2 m pixel⁻¹). We mapped the distribution of isolated boulders (86,896), rocky craters (3556), and rock exposures (7553) around potential Artemis landing sites 001 and 004 (NASA 2020), which are within or near one of the Artemis III candidate landing regions. We found that boulder abundance decreases with increasing distance from the rim of Shackleton crater. From that correlation, we infer that most of the boulders and rock exposures near Shackleton were deposited as ejecta by the Shackleton impact, and by later the reworking of that material during smaller impact events. We additionally assessed the accessibility of the mapped features, and documented geologic targets located on shallow (<15°) slopes, including those on the Shackleton crater rim and on the “Connecting Ridge” between Shackleton and Henson crater. Such targets could be sampled by a future mission to the lunar south pole region. Our catalog of mapped features is made available to the lunar community.

Unified Astronomy Thesaurus concepts: [Lunar science \(972\)](#); [Planetary geology \(2288\)](#); [Lunar impacts \(958\)](#); [Lunar craters \(949\)](#)

1. Introduction

The lunar south pole is located on the rim of Shackleton crater, a 21 km diameter simple crater created by an asteroid approximately 1.5 km in diameter (Zuber et al. 2012; Halim et al. 2021). Shackleton crater is of Imbrian age (3.43^{+0.04}_{-0.05} Ga, Spudis et al. 2008; Kring et al. 2021), and was excavated from a preexisting irregular massif, exposing blocks that may contain purest anorthosite on one side of the crater (PAN; Yamamoto et al. 2012; Gawronska et al. 2020), and a layered outcrop on the other side of the crater (Gawronska et al. 2020).

The massif connects Shackleton crater to Henson crater (known as Artemis III potential landing region “Connecting Ridge;” Glaser et al. 2014), which is thought to be of similar age to the nearby pre-Nectarian de Gerlache crater (Spudis et al. 2008). The massif has a maximum elevation of 1900 m, whereas the south pole on the rim of Shackleton crater has an elevation of 1290 m (Gawronska et al. 2020). It is thought that the massif was produced by the SPA basin forming impact

event along with several other massifs that occur along the southern topographic margin of the SPA basin (Spudis et al. 2008). Samples from within Shackleton ejecta blanket therefore could further the understanding of the SPA basin and SPA basin forming impact event, developing the geological understanding of the south polar region.

The south pole is surrounded by summits with high illumination that can provide access to solar power in a region that also contains permanently shadowed regions (PSRs) that may harbor volatile elements that can be used for crew consumables, radiation shielding, and propellant (e.g., Feldman et al. 2001; Colaprete et al. 2010; Paige et al. 2010; Hayne et al. 2015, 2021; Siegler et al. 2016; Li et al. 2018; Kring & Siegler 2019; Flahaut et al. 2020; Lemelin 2020; Lemelin et al. 2021). Those same volatile elements may provide clues about the volatile evolution of the solar system.

Deposits of water ice and other volatiles provide an opportunity to address numerous science objectives recognized as important by the lunar community (e.g., “The lunar poles are special environments that may bear witness to the volatile flux over the latter part of the solar system history;” National Research Council 2007; Crawford 2015; Pieters et al. 2018; Jawin et al. 2019). As a result, the south polar region of the



Original content from this work may be used under the terms of the [Creative Commons Attribution 4.0 licence](#). Any further distribution of this work must maintain attribution to the author(s) and the title of the work, journal citation and DOI.

Moon is an area of interest for multiple future missions, including the National Aeronautics and Space Administration's (NASA) Artemis program (NASA Artemis Program 2020), the Volatile Investigation Polar Exploration Rover (VIPER) mission (Colaprete et al. 2019), the European Space Agency's (ESA) PROSPECT instrument (Sefton-Nash et al. 2020; Heather et al. 2022), Indian Space Research Organisation's (ISRO) and Japanese Space Agency (JAXA) Lunar Polar Exploration (LUPEX) mission (Saiki et al. 2021), and the China National Space Agency's Chang'e program (Zhaoyu et al. 2015). Additionally, the south polar region is of interest for commercial missions such as NASA Commercial Lunar Payload Services (CLPS) missions (Atwell & Robinson 2020), ispace M1 and M2, and Intuitive Machines IM-1, IM-2, whose first mission IM-1 is to target the south pole region.

While the focus is often on volatile constituents in the south polar region, geologic materials within the area, such as isolated boulders, rock exposures, and rocky craters provide additional opportunities to address several other lunar exploration science objectives (National Research Council 2007), if sampled by astronauts during extravehicular activities (EVAs; e.g., Gawronska et al. 2020; Bernhardt et al. 2022). In this paper, we continue the geological mapping of the south pole, site 004 and site 001 initiated by Gawronska et al. (2020) and present an analysis of the distributions of 1. isolated boulders, 2. rock exposures, and 3. rocky craters.

1. Isolated material contained in boulders may originate from units that exist on steep slopes and/or topographic highs that would otherwise be inaccessible may also be found through mapping, and later collected during EVA. Samples collected at Station 6 from Boulder 2 at the Apollo 17 landing site are a good example of this, because high-resolution mapping of the boulder tracks from the sampled boulders showed that the boulders likely originated from outcrops within massif walls, providing context for the North/South Massif (Hurwitz & Kring 2016).
2. Rock exposures, may preserve distinct crustal lithologies and impact-generated features that could be explored during an EVA, and would provide new insights into the composition, chronology, and structure of the lunar crust, as well as information regarding impact flux on the Moon (e.g., National Research Council 2007). Large rock exposures akin to the rock exposures that exist in locations like the Schrödinger basin (e.g., Kring et al. 2016) and on the rim of Shackleton crater (Gawronska et al. 2020) were not found at the Apollo landing sites. Thus, new science opportunities are available to Artemis and other future missions at the south pole of the Moon.
3. Rocky craters, expose the subsurface, providing direct access to potentially distinct lithologies that would not be otherwise available for sampling. For example, on the EVA hike to Cone crater during Apollo 14, the Cone crater ejecta varied in composition, and in size from small particles to 10 m boulders, allowing a variety of samples from the Fra Mauro formation subsurface to be collected (Swann et al. 1977). Interestingly, one of the rock samples collected at Cone crater may contain the oldest fragment of the Hadean Earth (Bellucci et al. 2019; see Warren & Rubin 2020).

The regions mapped here each cover a 10 km radius (from the south pole and site 001 NASA Artemis plan; Figure A1), to represent the distance limit that may be traversed with an unpressurized rover, as during Apollo with its Lunar Roving Vehicle and as anticipated for future missions (e.g., Öhmann & Kring 2012; Allender et al. 2019). The mapped regions are centered on the lunar south pole and site 001 (defined by Bussey et al. 1999), and additionally mapping covers site 004 (defined by Bussey et al. 1999); furthermore, sites 001 and 004 are within one of the Artemis III candidate regions, known as the "Connecting Ridge" (Figure 1: 90°S, 0°W (south pole), 89.45°S, 137.31°W (site 001), and 89.78°S, 155.73°W (site 004)). Sites 001 and 004 were initially identified using Clementine data (sites A and B of Bussey et al. 1999) and then reexamined as points of significant illumination (sites 1 and 4 of Mazarico et al. 2011), before being tagged as 001 and 004 by NASA Artemis Program (2020). We discuss the distribution of the features in relation to the topography and the geomorphology of the south polar region. Our catalog of mapped features is made available to the community.

2. Data and Methods

2.1. Data Sets and Image Processing

Lunar Orbiter Laser Altimeter (LOLA) data (Smith et al. 2010) was used for topographic analysis. A LOLA 5 m pixel⁻¹ digital elevation model (DEM) with a corrected scaling factor of 0.5 was used to create a topography map of the south polar region (Figure 1). Hillshade and slope maps were derived from the LOLA DEM. Lunar Reconnaissance Orbiter Camera (LROC) Narrow Angle Camera (NAC) images (Chin et al. 2007; Robinson et al. 2010) with a resolution of ~0.5–2 m pixel⁻¹ were used to analyze and map the features within two exploration regions with a radius of 10 km (Figure A1). The United States Geological Survey (USGS) digital image processing software, Integrated Software for Imagers and Spectrometers 3 (ISIS3; e.g., Edwards 1987; Torson 1989; Edmundson et al. 2012) was used to process and project the NAC images with a lunar polar stereographic projection.

2.2. Identification of Isolated Boulders, Rocky Craters, and Rock Exposures

ArcMap (ArcGIS software, ESRI) was used for mapping isolated boulders, rock exposures, and rocky craters as individual points in separate shapefiles (e.g., Gawronska et al. 2020). Features were mapped on 109 individual NAC images, where images of varying illuminations and spatial resolutions occasionally overlapped (Figure A1 and Table A1). This approach was used to ensure that we mapped as many features as possible, including areas with short illumination periods. All features mapped were at least 2 × 2 pixels in size, which, considering the spatial resolution of the NAC images, includes only features that are greater than or equal to 1 to 4 m in diameter.

Following Gawronska et al. (2020), we mapped high albedo features that had a shadow in the opposite orientation to craters (in relation to the position of the Sun) as isolated boulders. Rock exposures are also generally composed of high albedo material, but were distinguishable from boulders because they are typically larger than individual boulders and create little to no shadow. Bowl-shaped depressions, with half of their wall exposed by incoming sunlight, were identified as rocky craters.

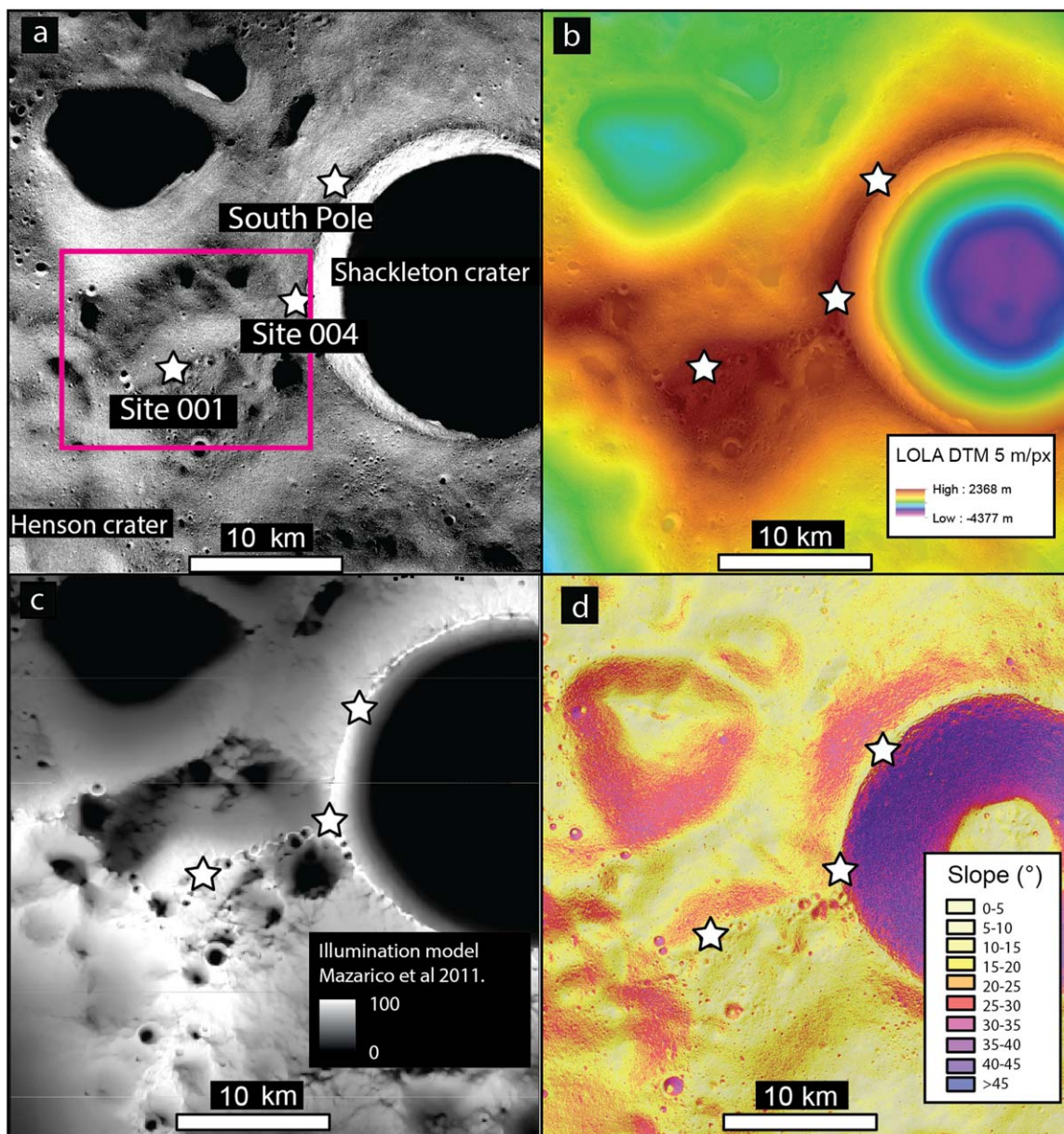


Figure 1. Context image showing location of the south pole and Shackleton crater; see Figure A1 for an outline of the region mapped here. White stars show the location of the south pole, site 001 (222.69°E, 89.45°S) and site 004 (204.27°E, 89.78°S). Pink square shows the location of the Artemis III candidate landing site, “Connecting Ridge”. (a)–(c) show the south pole and the points of interest of sites 001 and 004 in relation to Shackleton crater. (a) NAC mosaic (map assembled by Arizona State University and downloaded from Moon Trek (Day & Law 2018)) of the Shackleton region. (b) LOLA DEM (5 m pixel⁻¹) overlaid on a hillshade made using the LOLA DEM, showing the elevation of the Shackleton crater and surrounding region. (c) WAC illumination mosaic LROC. (d) Slope map overlaid on hillshade, both made using the LOLA (5 m pixel⁻¹) elevation data.

Rocky craters are typically surrounded with boulders, have high albedo ejecta and have a well-defined, uplifted rim, and are thus interpreted to be relatively younger in age (Thompson et al. 1974; Moore et al. 1980; Daubar et al. 2014). Density maps of the mapped features were created using the point density tool within ArcMap, where a cell size of 100 m and a search radius of 1000 km² was used.

2.2.1. Mapping Constraints

One of the main constraints of the geological mapping was the LROC NAC coverage. Due to the extreme illumination conditions, the large variation in the topography at the south pole, and seasonal changes, the distribution of illuminated

surfaces was often patchy (Bussey et al. 2010; Mazarico et al. 2011). In addition, LRO’s ground track has drifted away from the south pole over time, meaning that fewer pictures were taken directly over the south pole after ~2012, and those that were taken later were at a more oblique angle, reducing their resolution and making map projection and image alignment more difficult. Where possible, we relied on NAC images taken via the regular imaging mode and not the summed mode (where adjacent pixels have their values summed together to improve the signal to noise ratio, which reduces the image resolution), to maximize the number of images with higher spatial resolution. NAC mosaics of the south pole were not used in this study because of the limitations of these mosaics including suboptimal illumination and resolution.

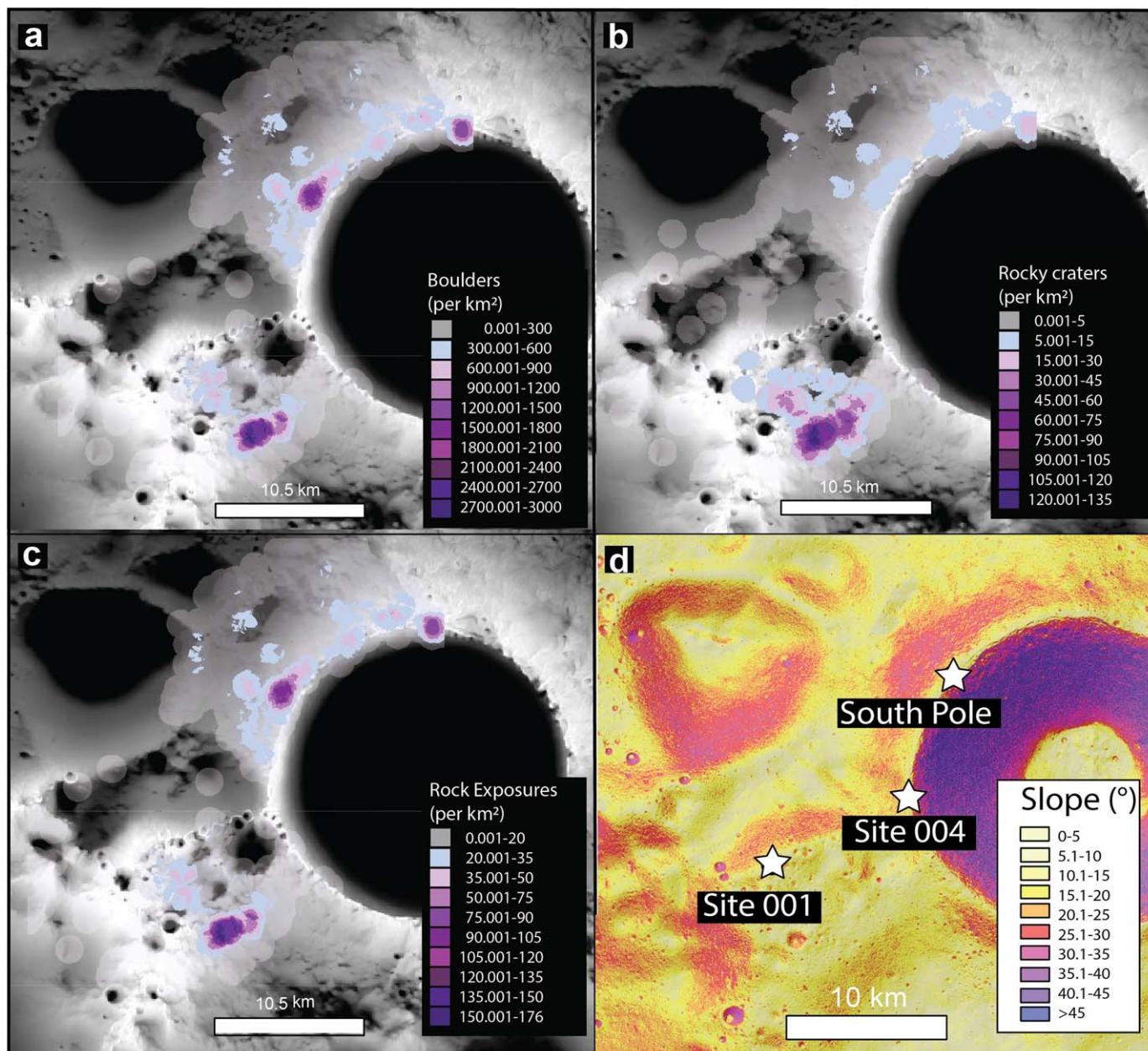


Figure 2. Density maps overlain on the illumination map by Mazarico et al. (2011). Density maps were created using a cell size of 100 m and a search radius of 1000 km². (a) Boulder distribution. (b) Rocky crater distribution (c) Rock exposures distribution. (d) LOLA derived slope map (5 m pixel⁻¹) to compare distribution with.

Mapping on individual, overlapping NACs increased variation of illumination direction and angle, thereby revealing more features that would otherwise have remained in shadow (Figure A1). However, this meant that the locations of features that were identified in different images might be spatially offset due to NAC georeferencing errors. This is because the NAC images used were map-projected, but the images were not bundle-adjusted (simultaneous refining of the 3D coordinates within the image) or orthorectified, which is a substantial effort for such a large region and beyond the scope of this work. The higher spatial resolution of the NAC images meant georeferencing to the LOLA DEM 5 m pixel⁻¹ would not be entirely accurate, and the size of the area mapped limited the possibility of georeferencing to NAC Digital Terrain Models (DTMs), due to the overall lack of NAC DTMs. All errors in our mapping can be reduced with ground-truthing efforts by future surface missions.

3. Results

3.1. Feature Distribution

Boulders were observed across the mapping area, with the highest densities concentrated along the rim of Shackleton crater and the “Connecting Ridge” between Shackleton and Henson craters (Figure 2(a)). Boulders are distributed evenly along the rim of Shackleton crater and boulder density reaches a maximum of 1800 boulders per km² along the Shackleton crater rim. As the distance from the Shackleton crater rim increases, boulder density decreases to 1–300 boulders per km² at the edge of the mapping region (Figure 2(a)). Additionally, we see a peak in the boulder distribution at the base of the “Connecting Ridge” slope (3000 boulders per km²) and then a decrease with distance from the ridge (Figure 2(a)). We observed that boulder sizes also vary with distance from the

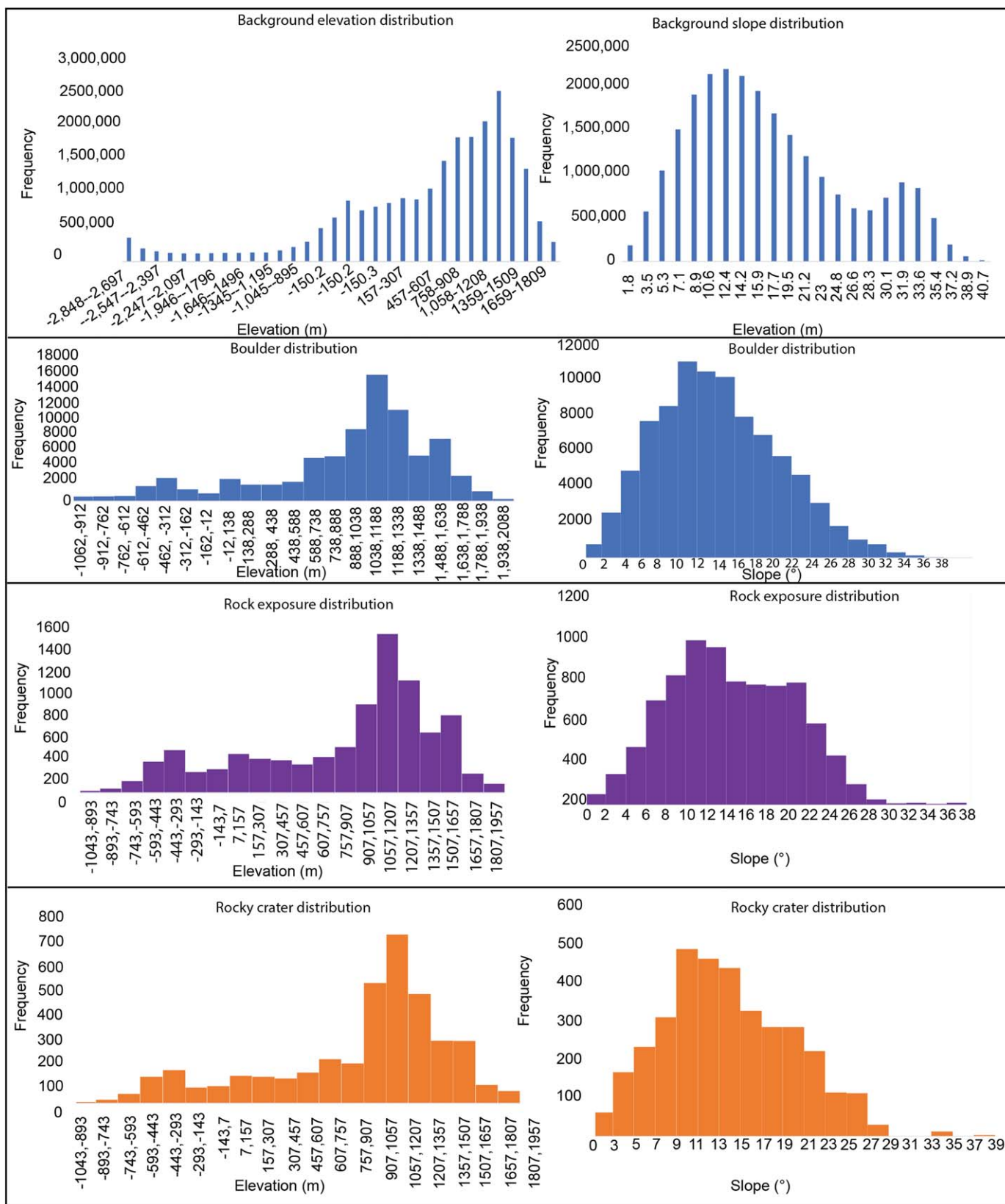


Figure 3. Histograms of the distribution of boulders, rock exposures, and rocky craters in relation to the elevation and the slopes.

Shackleton rim with larger boulders (~10 s m on average) found along the rim and decreasing in size with distance from Shackleton crater.

Rock exposures are seen across the mapping area, both near site 004, along the Shackleton crater rim, and atop the “Connecting Ridge” between Shackleton and Henson craters

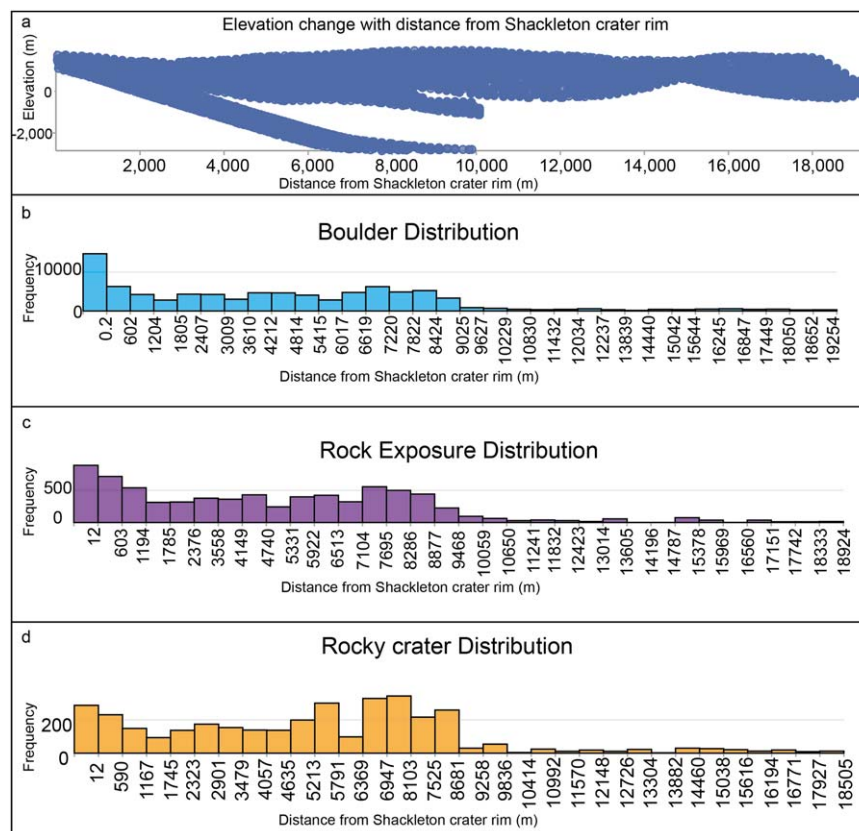


Figure 4. Distribution of features with distance from the Shackleton crater rim (a) scatter plot of the change in elevation with horizontal distance from Shackleton crater rim. (b) Distribution of boulders with distance from Shackleton crater rim. (c) Distribution of rock exposures with distance from Shackleton crater rim. (d) Distribution of rocky craters with distance from Shackleton crater rim.

(near site 001; Figure 2(c)). Similar, to the distribution of boulders, rock exposures were concentrated along the Shackleton crater rim with a maximum density of 90 rock exposures per km². Rock exposures are also abundant atop the “Connecting Ridge” between Shackleton and Henson craters, at a maximum density of 176 exposures per km². Rock exposures adjacent to the “Connecting Ridge” are significantly lower, <50 per km².

Similarly, the rocky craters are most concentrated atop the Shackleton–Henson “Connecting Ridge” near site 001, with 80 to 90 craters per km² (Figure 2(b)). The area most densely populated with rocky craters generally overlaps with the greatest clustering of rock exposures and boulders (Figure 2). Rocky craters are approximately uniformly distributed across the region surrounding the “Connecting Ridge”, with a maximum density of <135 rocky craters per km² (Figure 2(b)). The number of rocky craters on the Shackleton crater rim reaches a maximum of ~45 craters per km² near the south pole. Similarly, to boulders and exposures, fewer rocky craters are found with increasing distance from Shackleton and the “Connecting Ridge” (Figure 2(b)).

3.1.1. Distribution of Features in Relation to Elevation and Slopes

We observe some consistency in the distribution of the features investigated here, but most noticeably in the distribution of boulders, relative to slopes of <15° (Figures 2 and 3). The isolated boulders, rock exposures, and rocky craters are concentrated in areas of high elevation (>800 m), specifically along the rim of Shackleton crater and on the “Connecting Ridge” between Shackleton and Henson crater (Figures 2, 3, and 4).

At these elevations, boulders, rock exposures, and rocky craters appear to cluster on shallower slopes (<15°), like the flat rim of Shackleton crater, and the bottom of the exterior walls of Shackleton. There are clusters of all features on shallow slopes (<15°) near the “Connecting Ridge” between the Shackleton and Henson craters, but rocky craters occur on steeper slopes (>15°) as well (Figures 3 and 4).

3.2. Distribution of Boulders in Relation to PSRs

The distribution of boulders in relation to PSRs is shown in Figure 5. We observed that some of the large PSRs (i.e., Spudis crater) are located on the edge of the 10 km region surrounding the south pole and have small clusters of boulders close to and surrounding the extent of the PSR (~300–600 boulders per km²).

In the region surrounding the “Connecting Ridge”, there are fewer boulders close to the PSRs (~0–300 boulders per km², Figure 5(c)) consistent with our finding of fewer boulders with increasing distance from the Shackleton crater (Figure 4). In comparison, the PSRs on top of the “Connecting Ridge” are surrounded by relatively more boulders (~300–900 boulders per km², Figure 5(d)).

4. Discussion

4.1. Relationship of Isolated Boulders, Rock Exposures, and Rocky Craters, and their Distribution around Shackleton Crater

We observed a greater abundance of isolated boulders, rock exposures, and rocky craters closer to Shackleton crater and

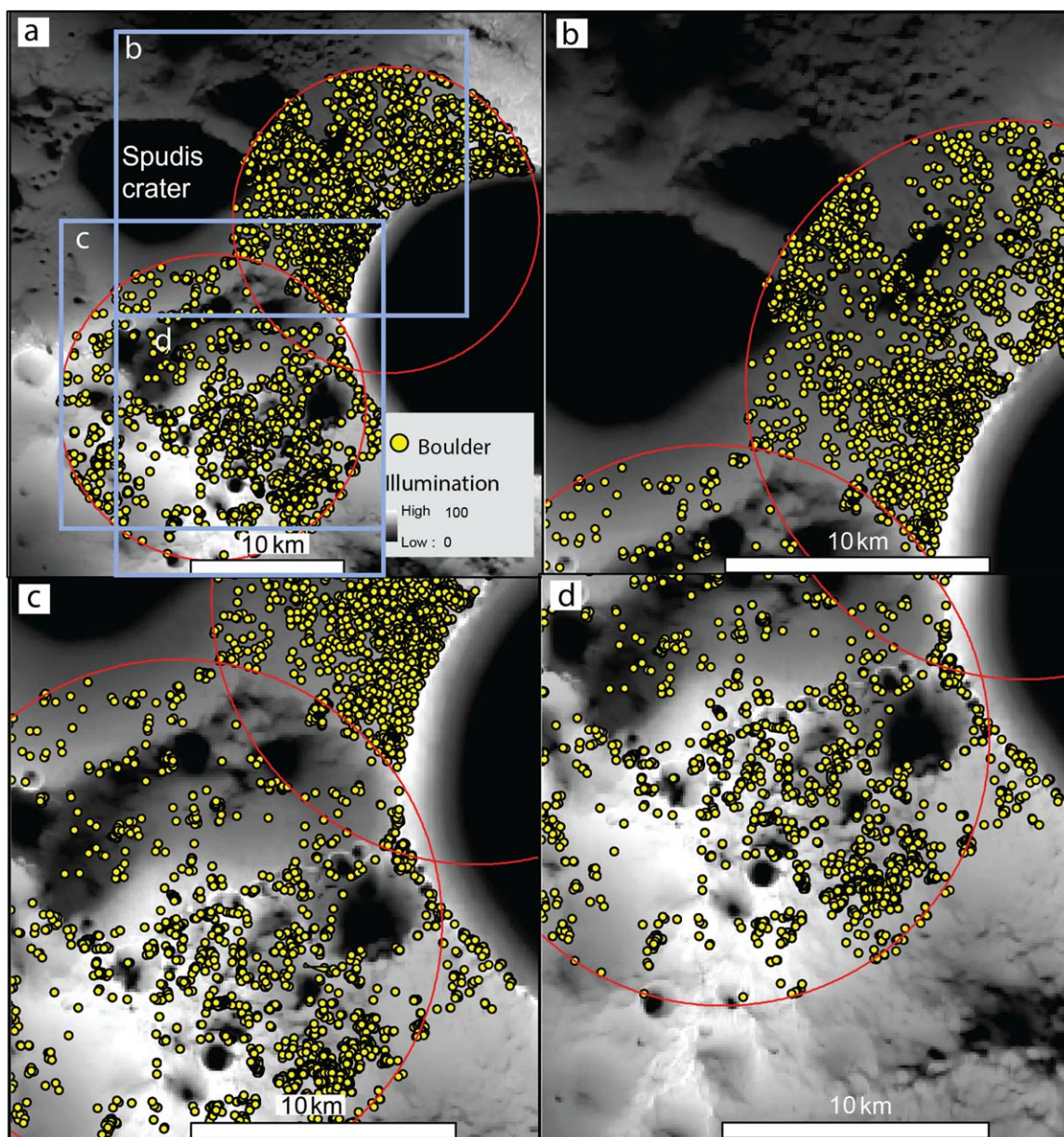


Figure 5. Boulder distribution in sunlit regions overlaid on a Wide Angle Camera (WAC) south pole illumination map from Mazarico et al. (2011) (100 m pixel^{-1}). (a) Context figure for (b)–(d). Red circles show the mapped area. Yellow points show the locations of individual boulders, and the blue squares show the locations of (b)–(d). (b) Distribution of boulders near large PSRs to the left of the image just on the edge of the mapping area. Bickel et al. (2021, 2022) found additional boulders in some of those PSRs (not shown here). (c) Boulder distribution across the “Connecting Ridge” area and fewer boulders seen surrounding the PSRs to the top of the image. (d) Boulder distribution to the base of the “Connecting Ridge” slope, more boulders seen surrounding the PSRs that cover crater floors.

on the “Connecting Ridge” between Shackleton and Henson craters. Moreover, there is a systematic decrease in the number of boulders with increased distance from Shackleton crater rim (Figure 4). It is possible that most of the boulders and rock exposures mapped are ejecta from Shackleton crater, particularly the boulders that are located on the crater rim. Larger boulders are found on and near the Shackleton rim, but with distance from the rim we found smaller boulders, similar to the findings of Watkins et al. (2019) and Bart & Melosh (2010) who mapped six small craters near legacy landing sites (Apollo 16, Apollo 14, Apollo 16, Chang’e-3, Apollo 17, and Apollo 12) and 18 craters that are hundreds of meters in diameter, respectively. If these boulders are ejecta from the Shackleton impact, then they are either recently exposed portions of the ejecta blanket, they are relics of much larger

boulders, or their degradation rates are unusually slow because they have survived 3.43 Ga. Previous studies observing boulders of $>2 \text{ m}$ from smaller craters (150–950 m diameter) suggest survival times of 40–80 Ma (Basilevsky et al. 2013) and less than $<200 \text{ Ma}$ for craters less than a 1 km (Watkins et al. 2019). Because Shackleton crater is much larger in diameter and would have, therefore, produced larger boulders (\sim up to 10 s m) with boulder excavation size related to the crater size (Gault et al. 1963; Muehlberger et al. 1972; Watkins et al. 2019). Thus, the boulders observed could be degraded boulders from the Shackleton impact. On the other hand, the boulders could be from younger impact events in the area (Tye et al. 2015). Evidence for these younger events is seen by the number of rocky craters observed and boulder fields on or close to the

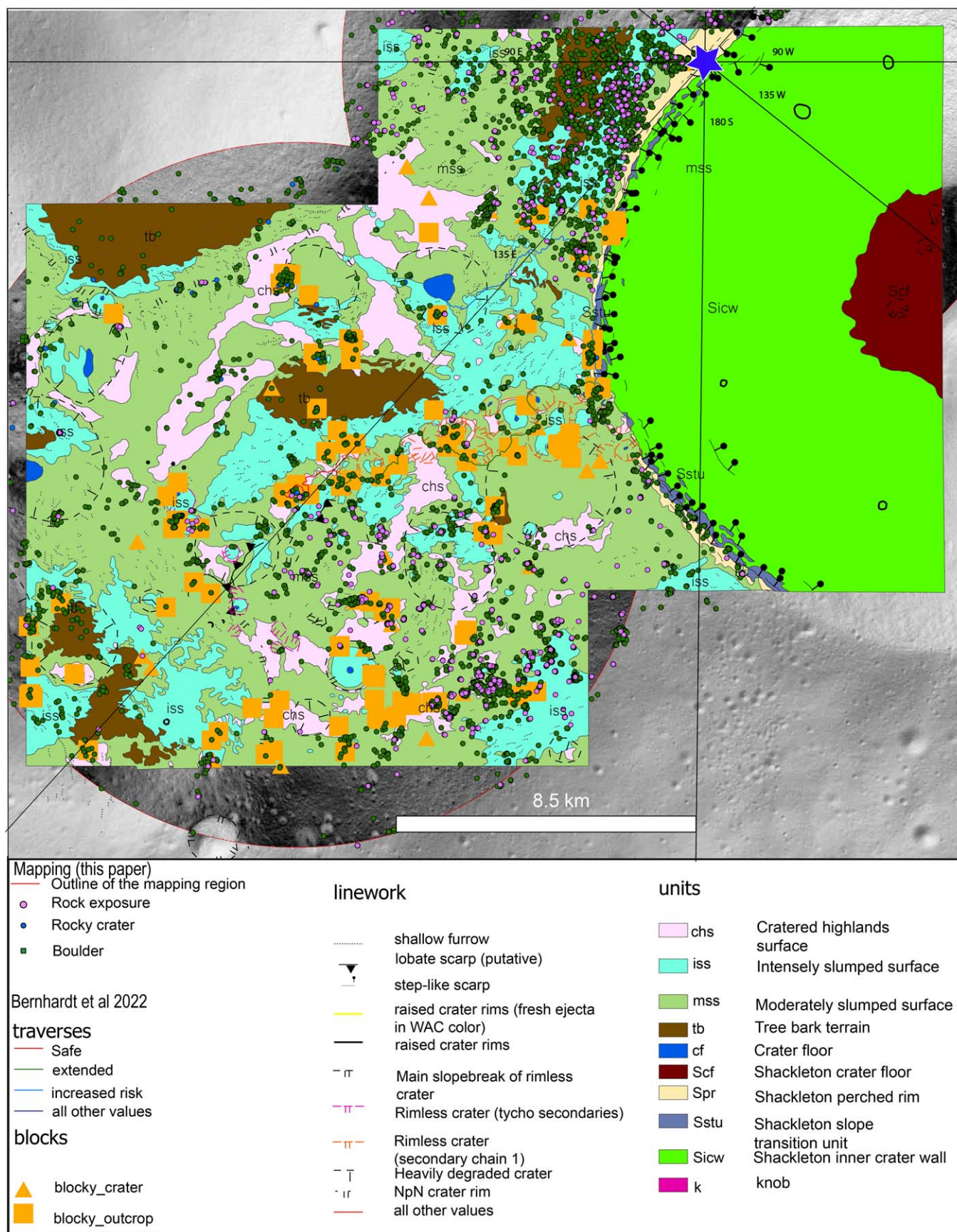


Figure 6. Features mapped (isolated boulders, rock exposures, rocky craters) overlaid on the Bernhardt et al. (2022) geomorphological map. Distribution of features in relation to the geomorphic units can be seen, including around the “Connecting Ridge” the moderately slumped unit aligns with the mapped features. Blue star shows the location of the south pole (90°S) and longitude lines marked.

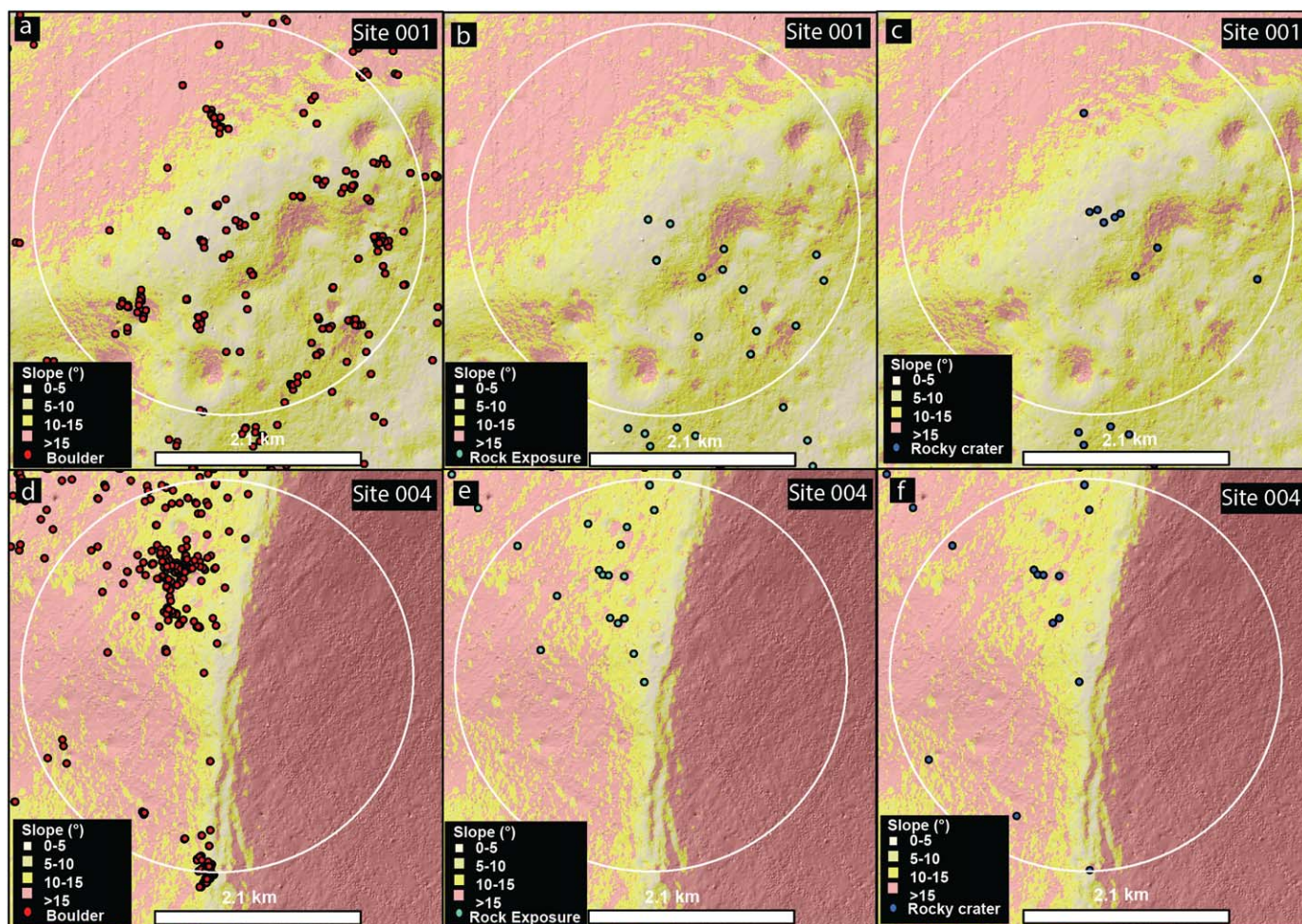


Figure 7. 2 km exploration zones around sites 001 and 004 shown on LOLA (5 m pixel^{-1}) derived slope maps overlaid on a LOLA derived hillshade. (a)–(c) shows the exploration zone around site 001. Scale bars in all panels are 2.1 km long. (a) Boulder distribution in relation to slopes. (b) Rock exposure distribution in relation to slopes. (c) Rocky craters in relation to slopes. (d)–(f) shows the 2 km ellipse around site 004. (d) Boulder distribution in relation to slopes. (e) Rock exposure distribution in relation to slopes. (f) Rocky craters in relation to slopes.

Shackleton rim (Figure 3; Tye et al. 2015). Young events may have generated at least some of the as-yet uneroded small boulders. The dominant lithology in this area is likely represented by the small boulders and is probably dominated by reworked SPA ejecta, which could be itself reworked SPA ejecta (Spudis et al. 2008). An additional consideration at the south pole is that if a crater is produced in a region with icy regolith, the impact might produce a different ejecta distribution than a crater in a regolith without ice (e.g., Rubanenko et al. 2019; Cannon et al. 2020b). Furthermore, boulders that are composed of icy regolith and are brought to the surface, potentially in sunlight, with higher temperatures may degrade faster than boulders without ice. This should be a consideration particularly when sampling boulders from or near PSRs (Figure 5). Further away from the Shackleton crater rim, we observe still, that the distribution of boulders and rocky craters closely aligns (Figure 4), suggesting that the boulders that surround these rocky craters are likely ejecta from smaller impact events that exposed subsurface lithologies within the south polar region (e.g., Deutsch et al. 2020a, 2020b). While Gawronska et al. (2020) found possible layers of ejecta exposed in the Shackleton crater inner wall, no clear layering features were observed within the boulders or the rock exposures mapped here. This

may be due to the resolution of mapping, which was at the coarsest 2 m pixel^{-1} . Alternatively, it may be because we were observing isolated features rather than larger outcrops, where distinct formations may be more readily visible.

There is a large number of rocky craters at the base of the “Connecting Ridge” slope between Shackleton and Henson craters. Their greater abundance at the bottom of the “Connecting Ridge” relative to the plains on either side of the “Connecting Ridge” may suggest that the substrate here differs to the plains and the Shackleton rim. It is possible that the “Connecting Ridge” is only thinly covered in regolith, so it is more likely to preserve rocky craters, and may be more friable, whereas the rim is covered with more ejecta, and the plains less regolith (e.g., Kring et al. 2020). There remains, however, a level of uncertainty in geologic conditions in the area. Asymmetries in the morphology of Shackleton crater may have been produced by subsurface ice in the target (Halim et al. 2021). If icy regolith persists in the region, then it may affect conditions along the “Connecting Ridge” and Shackleton crater and, therefore, the distribution of rocky craters (Colaprete et al. 2012; Cannon & Britt 2020a).

Overall, there is a greater number of boulders, rock exposures, and rocky craters near the rim of Shackleton crater and the frequency of each of these features decreases with

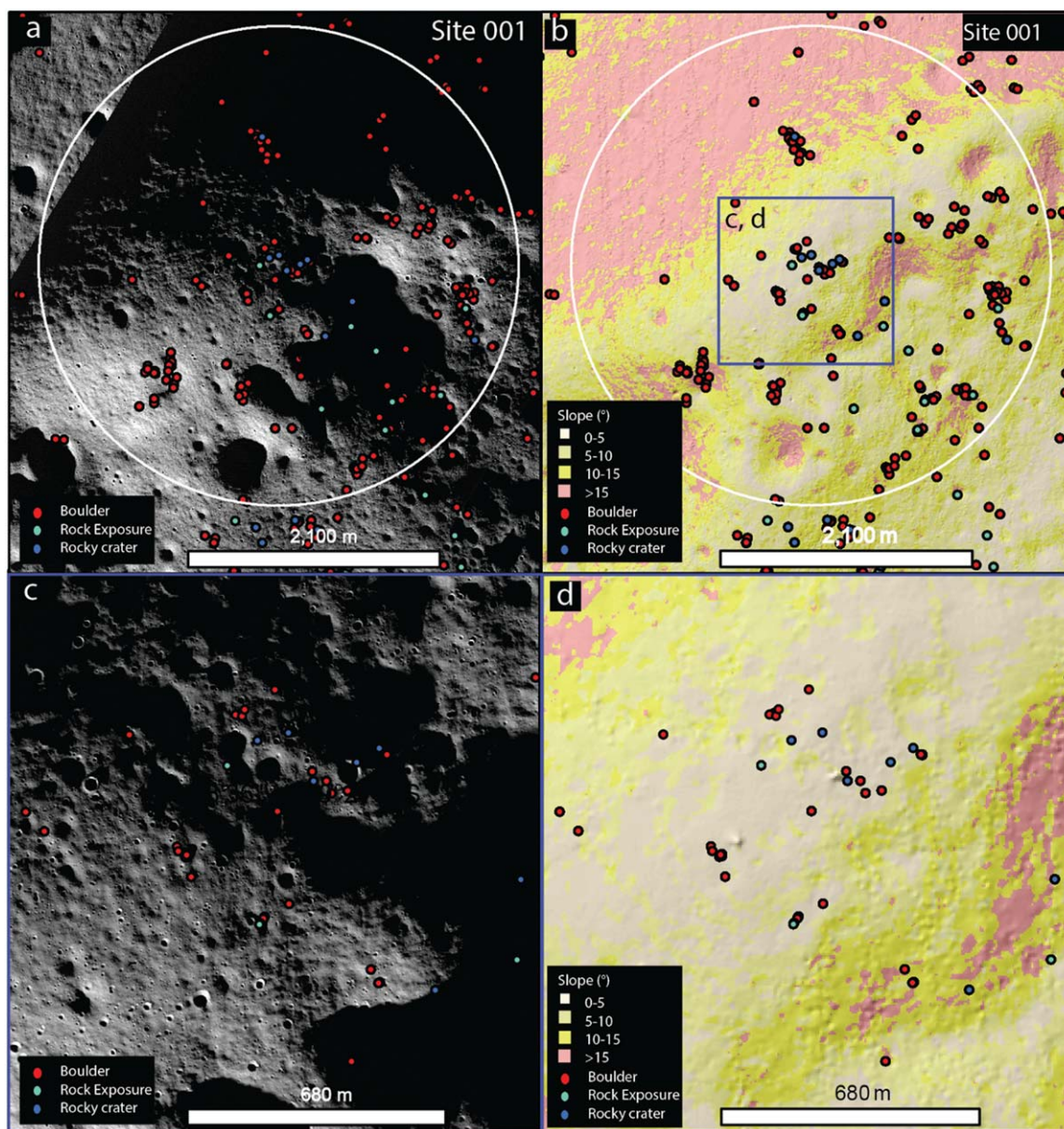


Figure 8. (a) 2 km exploration zone around site 001 shown on NAC mosaic (1 m pixel^{-1}), all features shown. (b) 2 km exploration zone on LOLA (5 m pixel^{-1}) derived slope map, blue box shows the extent of (c) and (d) which is a more accessible region with slopes of less than 10° . Scale bars in (a) and (b) are 2400 m and scale bars in (c) and (d) are 680 m. (c) NAC mosaic at more accessible area within the site 001 exploration zone. (d) Detail of the LOLA derived slope map.

distance from Shackleton crater rim. As a result, there is greater opportunity to collect crystalline material along the Shackleton rim or the “Connecting Ridge” during a future mission to this region, as compared with more distant locations in the Shackleton ejecta deposit. Additionally, Shackleton crater lies on the edge of the South Pole-Aitken basin, which may have exposed either shallow or deep crustal lithologies (Pieters et al. 1997, 2001; Borst et al. 2012; Vaughan & Head 2014; Hurwitz & Kring 2015; Moriarty & Pieters 2018). Any boulders sampled from the rim of Shackleton and or near the “Connecting Ridge” between Shackleton and Henson craters may therefore be either anorthositic (representing the shallow crust) or noritic (representing the deep crust) in composition and could originate from crustal lithologies that formed during the Lunar Magma Ocean (e.g., Lemelin et al. 2022). We found that one location atop the “Connecting Ridge” between

Shackleton and Henson craters, presents clusters of rocky craters, rock exposures, and boulders (see Figures 2 and 4). This is near to site 001 and one of the Artemis III candidate landing regions and may be an ideal target for future sampling activities where a large number of features could be sampled over a short distance. This type of exploration would further allow for detailed examination of the lithological characteristics of this area and would provide geological context for the collection of any potential resources necessary to sustain a human habitat, should this site be targeted in the future for a permanent lunar surface outpost (e.g., Crawford 2015).

4.2. Geomorphology

Bernhardt et al. (2022) mapped the geomorphology around the “Connecting Ridge” between Shackleton and Henson craters, classifying the surface into different geomorphological

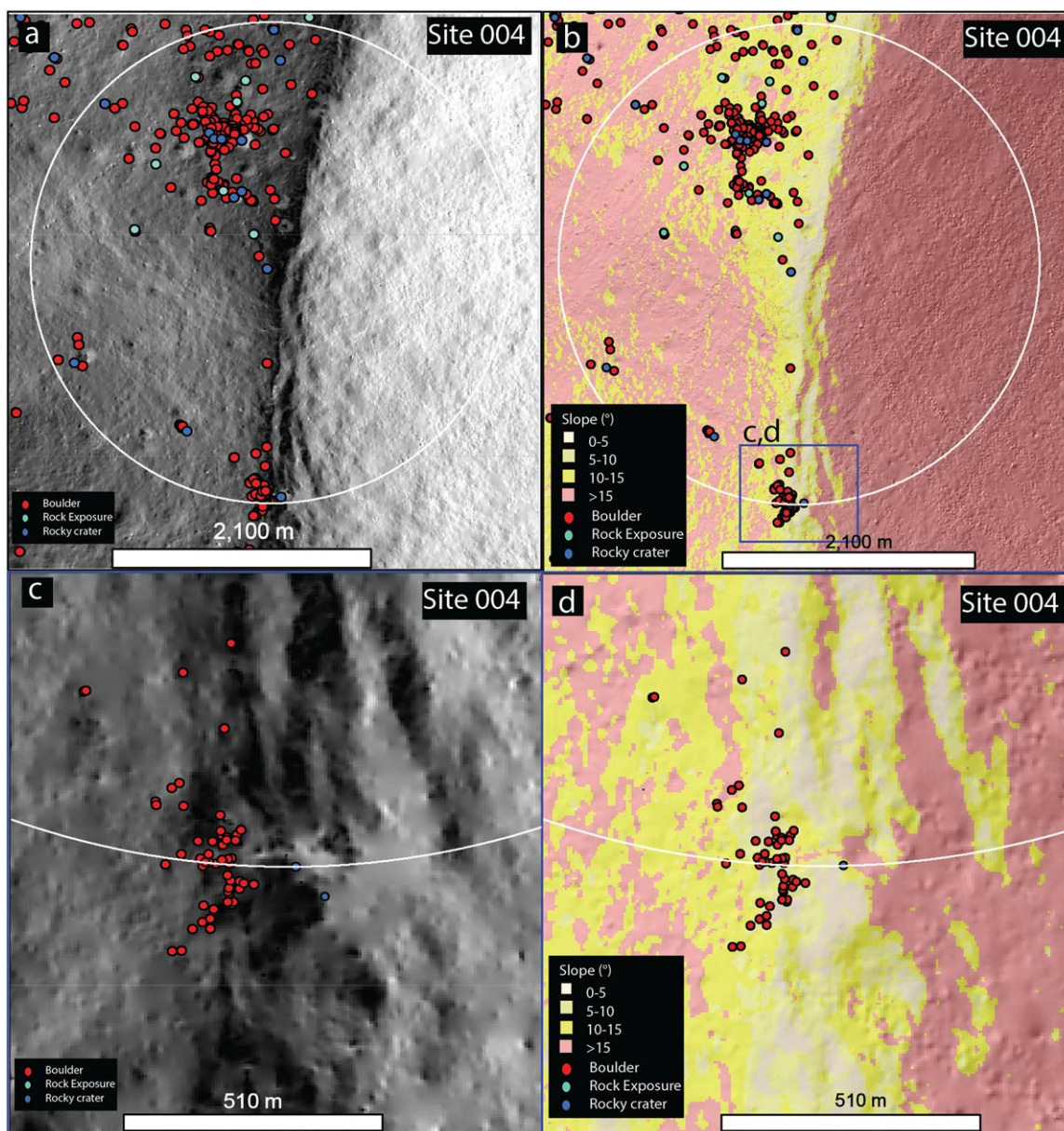


Figure 9. (a) 2 km exploration zone around site 004 shown on NAC mosaic (1 m pixel^{-1}), all features shown. (b) 2 km exploration zone on LOLA (5 m pixel^{-1}) derived slope map. The blue box shows the extent of c and d which are more accessible region with slopes less than 10° . (c) NAC mosaic at an accessible area within the ellipse. (d) Detail of the LOLA derived slope map. Scale bars in (a) and (b) are 2100 m and those in (c) and (d) are 510 m.

units at a scale of 1:8000 (Figure 6). The greatest clustering of boulders and rock exposures found here aligns with the unit “moderately slumped surface texture”, as described by Bernhardt et al. (2022) (Figure 6). We observed less boulders around the “Connecting Ridge” region in areas where Bernhardt et al. (2022) describe the geomorphology as an “intensely slumped textured surface”, where steeper slopes exist, which could allow boulders to roll down instead of settling. These surface textures indicate that there is a relationship between the distribution of boulders and rock exposures and slopes where boulders are more concentrated on shallower slopes ($<15^\circ$) possibly due to processes such as slumping and creep (e.g., Verrall & O’Connell 1979; Zuber et al. 2012; Xiao et al. 2013). Slumping and creep cause changes to the steepness of crater walls, ridges, and plateaus, probably including those within the region around Shackleton (e.g., Bernhardt et al. 2022; Zuber et al. 2012). As outlined in

Section 3.1.1, boulders and rock exposures are concentrated on relatively lowland plains with low slopes. Boulders also collected at the base of slopes or topographic low elevations, similar to the Station 2 and 6 boulders at the Apollo 17 landing site (Hurwitz & Kring 2016).

In comparison, rocky craters appear to follow the “cratered highlands surface” defined by Bernhardt et al. (2022) (Figure 6). Nearer Shackleton crater, the feature distribution follows less closely with the geomorphic units outlined by Bernhardt et al. (2022) (Figure 6).

4.3. Accessibility of Features

Mapping isolated boulders, rock exposures, and rocky craters revealed many geologic targets that are available for sampling within 2 km radii, the distance defined possible for a walking EVA (Öhmann & Kring 2012; Allender et al. 2019)

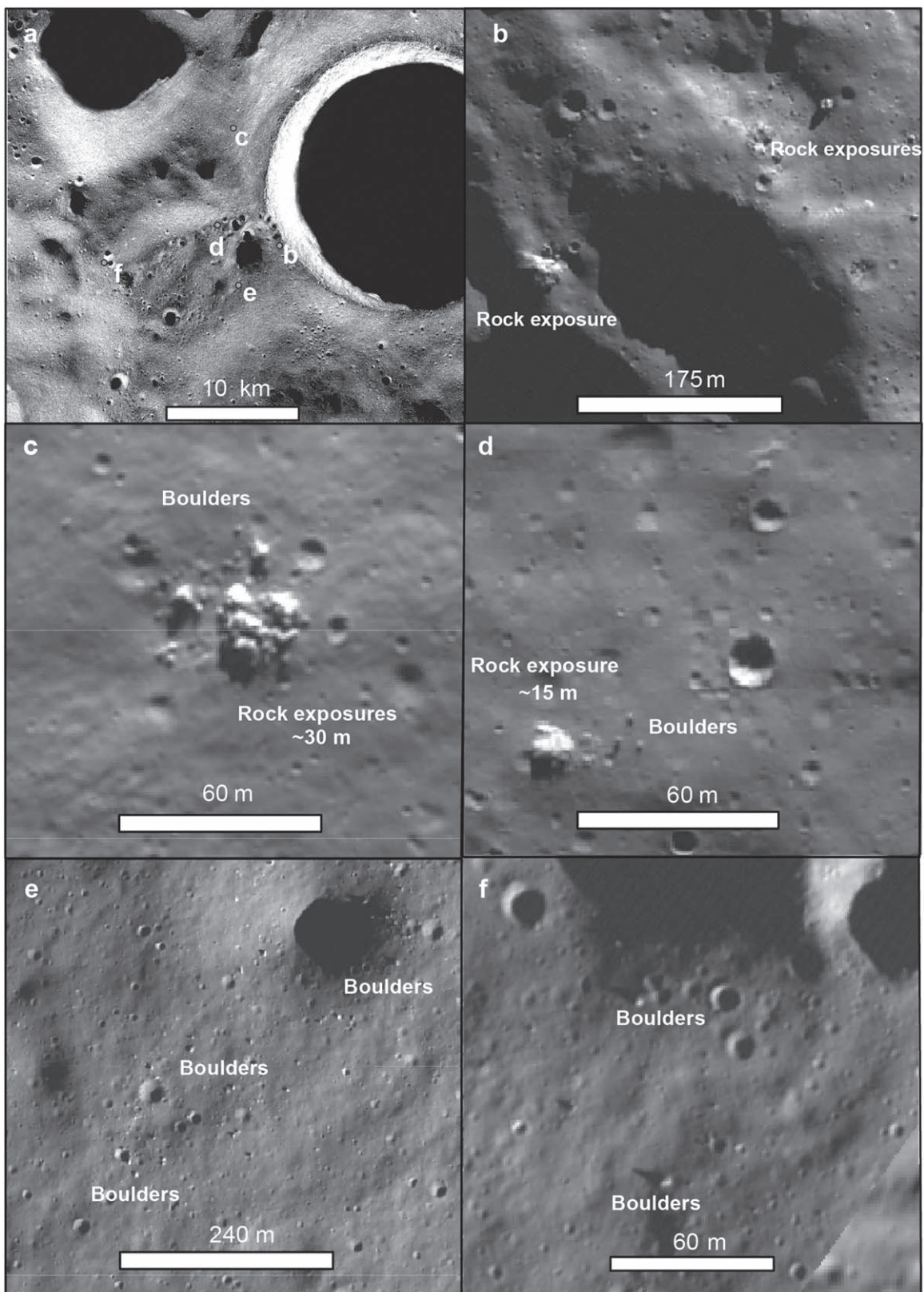


Figure 10. Examples of boulders and rock exposures that are within/in near proximity to the Artemis III candidate regions and therefore are of potential interest for sampling. (a) context image of where (b)–(f) are located. (b) Rock exposures on the rim of Shackleton crater. (c) Rock exposures and boulders just above the ridge. (d) Rock exposure and boulders. (e) Boulder field. (f) Large boulders.

around sites 001 and 004, and therefore suitable for sampling with the Artemis III mission for which an unpressurized rover is not planned.

Two of the constraints of an EVA activity and/or for landing a rover/lander are illumination conditions and Earth visibility. Both sites 001 and 004 have high illumination conditions and,

therefore, are suitable places to identify accessible features (e.g., Mazarico et al. 2011). The “Connecting Ridge” near site 001 has small areas that meet the requirements of the Artemis III human landing system (Kring et al. 2022). Figure 7 shows several examples of 2 km diameter exploration zones. Within this 2 km region we observed an abundance of features around sites 001 and 004, in proximity to Artemis III candidate landing region known as the “Connecting Ridge” (Figure 1), making these sites great targets for sampling. Notably, a number of boulders are in close proximity to rocky craters, providing the opportunity to correlate boulders with potentially known sources. Two particularly accessible sites are shown in Figures 8 and 9, where slopes average less than 0° – 10° for both sites 001 (Figures 8(c)–(d)) and 004 (Figures 9(c)–(d)). From the features observed at sites 001 and 004, site 001 contains a greater frequency of features which could be sampled.

Additionally, Figure 10 shows examples of rock exposures and boulders that are within or in near proximity to the Artemis III candidate landing region known as the “Connecting Ridge”, and these examples are features which could be sampled.

4.3.1. Recent Erosional Activity

Within the south polar region (85° S and southward) 84 boulder tracks have been detected, and 13 additional ones were found to enter Shackleton crater (Bickel & Kring 2020). Some of those boulders were displaced along the rim of Shackleton crater (not downslope), likely having been produced by a nearby, small impact crater.

Some of the tracks that enter Shackleton crater could not be traced completely due to the PSR; there may be more tracks that are not visible (see e.g., Sargeant et al. 2020 for low latitude PSRs).

Although sites 001 and 004 make suitable sites for future missions and EVAs, there is evidence of boulder displacement within the south polar region and Bickel & Kring (2020) one of the boulder tracks identified by Bickel & Kring (2020), with a length of ~ 520 m, is located within our south pole exploration zone mapping area. The tracks suggest there is geologically recent erosional activity, which should be a consideration for future missions, particularly when traversing and/or operating on or below steep slopes. Although a boulder track was found within the mapping area, it is likely that most boulders rolled more than 25 Myr ago based on the ages of the Apollo 17 landing site (Arvidson et al. 1975; Hurwitz & Kring 2016; Kumar et al. 2016). Additionally, we observed thousands of boulders suggesting that boulder displacement during a future mission in the next 5–10 yr is unlikely.

5. Conclusions

Isolated boulders, rock exposures, and rocky craters are mapped within a 10 km radius from the south pole and from site 001 on the “Connecting Ridge” between Shackleton and Henson craters and additionally cover the Artemis III candidate landing regions. A greater density of boulders occurs closer to the rim of Shackleton crater, which likely corresponds to the Shackleton impact event that occurred ~ 3.43 Ga. Fewer features were observed on steeper slopes ($>15^{\circ}$) supporting

previous mapping efforts in the south polar region (e.g., Gawronska et al. 2020; Bernhardt et al. 2022). Additionally, we have highlighted areas which are accessible and shown the distribution of features within these accessible areas. Investigations of the lunar south polar region should continue to assess the accessibility of features of interest, including isolated boulders, rock exposures, rocky craters, and PSRs, in preparation for upcoming missions to the area. Such investigations will provide crucial context for any future endeavors set to explore the south pole of the Moon. Acknowledgements

The catalog of mapped features will be made available to the community. We acknowledge NASA/LROC/GSFS/ASU for the NAC images used in this study. We also thank the staff of the Lunar and Planetary Institute for their support during a 2019 Exploration Science internship through the Center for Lunar Science and Exploration, where part of this work was completed. This work was supported by NASA Solar System Exploration Research Virtual Institute contracts NNA14AB07A and 80NSSC20M0016. LPI Contribution No. 2868. LPI is operated by USRA under a cooperative agreement with the Science Mission Directorate of NASA.

Appendix

This appendix contains Figure A1, which shows the mapping area and highlights the number of NAC images used. Additionally, we include Table A1, which contains the NAC IDs used.

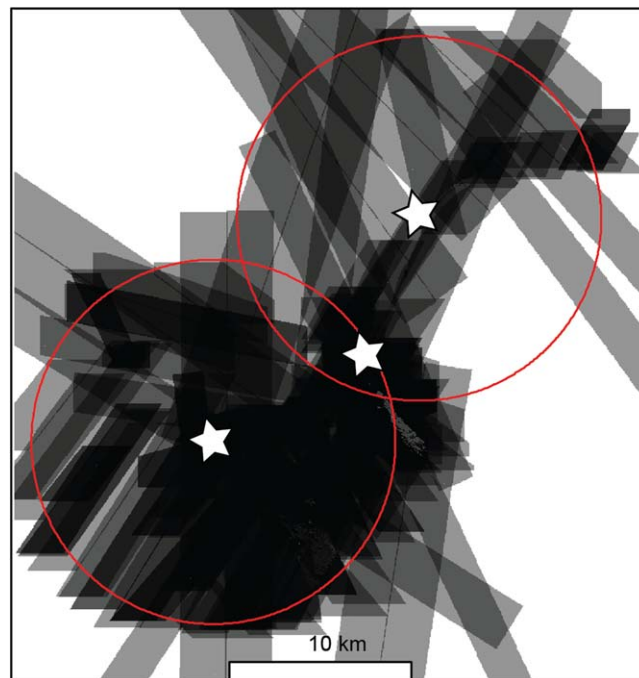


Figure A1. NAC image coverage over the mapping area. Red circles show the mapping region, and the gray boxes show the footprints of the 109 NAC images used. Darker areas show where several NACs overlap, covering the same area.

Table A1
List of the NAC Images Used in the Feature Mapping

NAC ID
M140924004LE
M140924004RE
M140903652RE
M140883298RE
M140903652LE
M131431751RE
M140876512RE
M140876512LE
M140883298LE
M140883298RE
M106922302RE
M133758902RE
M131445318RE
M131445318LE
M131418183RE
M128269681LE
M128269681RE
M118721097RE
M104027535LE
M143276169RE
M133772465LE
M143291733LE
M143251041RE
M143264605LE
M143264605RE
M143223911LE
M143237476LE
M140849369LE
M140849369RE
M143210345LE
M131458885LE
M133786042RE
M133799601LE
M140835795RE
M118673590RE
M132015106LE
M132015106RE
M132028670RE
M139783961LE
M139783961RE
M139858589LE
M140068959LE
M140197843LE
M140197843RE
M142416660RE
M146833333LE
M146928260LE
M146928260RE
M147219735LE
M147253633LE
M140136780RE
M140136780LE
M128269681LE
M118721097LE
M118721097RE
M107037007LE
M106922302RE
M104027535LE
M133758902RE
M131458885LE
M131445318RE
M131445318LE
M131431751RE
M142348843LE
M133840314LE

Table A1
(Continued)

NAC ID
M101271659RE
M104027535LE
M133053226LE
M133813180LE
M131458885LE
M128357891RE
M128344319RE
M128344319LE
M128269681RE
M118721097LE
M112504292RE
M103870068RE
M112504292RE
M133786042LE
M118673590LE
M118673590RE
M140862941RE
M140862941LE
M140849369RE
M140849369LE
M140835795RE
M140835795LE
M130644650RE
M128330747RE
M128330747LE
M103805633RE
M103805633LE
M102467116LE
M101493578RE
M101493578LE
M169678331RE
M169644422RE
M169644422LE
M169610511LE
M102467116LE
M101493578LE
M142586221LE
M142572660RE
M142572660LE
M132001536RE
M132001536LE
M131987966RE
M140862941RE
M140862941LE

ORCID iDs

Sarah. J. Boazman  <https://orcid.org/0000-0003-4694-0818>
Animireddi V. Satyakumar  <https://orcid.org/0000-0002-7893-3199>

References

- Allender, E. J., Orgel, C., Almeida, N. V., et al. 2019, *AdSpR*, **63**, 692
Arvidson, R., Crozaz, G., Drozd, R. J., Hohenberg, C. M., & Morgan, C. J. 1975, *Moon*, **13**, 259
Atwell, M., & Robinson, M. S. 2020, LPI Contribution, 2241, 6011
Bart, G. D., & Melosh, H. J. 2010, *Icar*, **209**, 337
Basilevsky, A. T., Head, J. W., & Horz, F. 2013, *P&SS*, **89**, 118
Bellucci, J. J., Nemchin, A. A., Grange, M., et al. 2019, *E&PSL*, **510**, 173
Bernhardt, H., Robinson, M. S., & Boyd, M. 2022, *Icar*, **379**, 114963
Bickel, V., & Kring, D. 2020, *Icar*, **348**, 113850
Bickel, V. T., Moseley, B., Hauber, E., et al. 2022, *GeoRL*, **49**, e99530

- Bickel, V. T., Moseley, B., Lopez-Francos, I., & Shirley, M. 2021, *NatCo*, **12**, 5607
- Borst, A. M., Foing, B. H., Davies, G. R., & van Westrenen, W. 2012, *P&SS*, **68**, 76
- Bussey, D. B. J., McGovern, J. A., Spudis, P. D., et al. 2010, *Icar*, **208**, 558
- Bussey, D. Ben J., Spudis, Paul D., & Robinson, Mark S. 1999, *GeoRL*, **26**, 1187
- Cannon, K. M., & Britt, D. T. 2020a, *Icar*, **347**, 113778
- Cannon, K. M., Deutsch, A. N., Head, J. W., & Britt, D. T. 2020b, *GeoRL*, **47**, e88920
- Chin, G., Brylow, S., Foote, M., et al. 2007, *SSRv*, **129**, 391
- Colaprete, A., Andrews, D., Bluethmann, W., et al. 2019, *AGUFM*, **P34B-03**
- Colaprete, A., Elphic, R. C., Heldmann, J., et al. 2012, *SSRv*, **167**, 3
- Colaprete, A., Schultz, P., Heldmann, J., et al. 2010, *Sci*, **33**, 463
- Crawford, I. A. 2015, *PrPG*, **39**, 137
- Daubar, I. J., Atwood-Stone, C., Byrne, S., McEwen, A. S., & Russell, P. S. 2014, *JGRE*, **119**, 2620
- Day, B., & Law, E. 2018, *COSPAR*, **42**, B3.1-11-18
- Deutsch, A., Head, J., & Neumann, G. 2020a, *Icar*, **336**, 113455
- Deutsch, A., Head, J., Neumann, G., Kreslavsky, M., & Barker, M. 2020b, *GeoRL*, **47**, e87782
- Edmundson, K. L., Cook, D. A., Thomas, O. H., Archinal, B. A., & Kirk, R. L. 2012, *ISPan*, **1-4**, 203
- Edwards, K. 1987, *PgERS*, **53**, 1219
- Feldman, W. C., Maurice, S., Lawrence, D. J., et al. 2001, *JGR*, **106**, 23231
- Flahaut, J., Carpenter, J., Williams, J.-P., et al. 2020, *P&SS*, **180**, 104750
- Gault, D., Shoemaker, G., & Moore, H. 1963, Spray Ejected from the Lunar Surface by Meteoroid Impact, NASA TN D-1767, Ames Research Center, <https://ntrs.nasa.gov/citations/19630004711>
- Gawronska, A., Barrett, N., Boazman, S., et al. 2020, *AdSpR*, **66**, 1247
- Gläser, P., Scholten, F., De Rosa, D., et al. 2014, *Icar*, **243**, 78
- Halim, S. H., Barrett, N., Boazman, S. J., et al. 2021, *Icar*, **354**, 113992
- Hayne, P. O., Aharonson, O., & Schörghofer, N. 2021, *NatAs*, **5**, 169
- Hayne, P. O., Hendrix, A., Sefton-Nash, E., et al. 2015, *Icar*, **255**, 58
- Heather, D., Fissackerly, R., & Trautner, R. 2022, *EPSC*, **16**, EPSC2022-533
- Hurwitz, D., & Kring, D. A. 2015, *E&PSL*, **427**, 31
- Hurwitz, D., & Kring, D. A. 2016, *E&PSL*, **436**, 64
- Jawin, E. R., Valencia, S. N., Watkins, R. N., et al. 2019, *E&SS*, **6**, 2
- Kring, D., Bickel, V. T., Fagan, A. L., et al. 2022, in Assessing landing and EVA options in the vicinity of potential Artemis landing 001, NASA Exploration Science Forum
- Kring, D., Kramer, G. Y. D., Bussey, B. J., et al. 2021, *AdSpR*, **68**, 4691
- Kring, D., Siegler, M., & Paige, D. 2020, *LPSC*, **51**, 1933
- Kring, D. A., Kramer, G. Y., Collins, G. S., Potter, R. W. K., & Chandnani, M. 2016, *NatCo*, **7**, 13161
- Kring, D. A., & Siegler, M. A. 2019, Diachotomy of Science and ISRU Targets, Annual Meeting of the Lunar Exploration Analysis Group 2019, Abstract No. 5007
- Kumar, S. P., Sruthi, U., Krishna, N., et al. 2016, *JGRE*, **121**, 147
- Lemelin, M. 2020, *LPSC*, **51**, 1197
- Lemelin, M., Li, S., Mazarico, E., et al. 2021, *PSJ*, **2**, 103
- Lemelin, M., Lucey, P. G., & Camon, A. 2022, *PSJ*, **3**, 63
- Li, S., Lucey, P. G., Miliken, R. E., et al. 2018, *PNAS*, **115**, 8907
- Mazarico, E., Neumann, G. A., Smith, D. E., Zuber, M. T., & Torrence, M. H. 2011, *Icar*, **211**, 1066
- Moore, H. J., Boyce, J. M., & Hahn, D. A. 1980, *M&P*, **23**, 231
- Moriarty, D. P., III, & Pieters, C. M. 2018, *JGRE*, **123**, 729
- Muehlberger, W. R., Batson, R. M., Boudette, E. L., et al. 1972, Preliminary geologic investigation of the Apollo 16 landing site, NASA SP-315, NASA, <https://pubs.er.usgs.gov/publication/70042871>
- NASA Artemis Program 2020, NASA's Plan for Sustained Lunar Exploration and Development, NASA, https://www.nasa.gov/sites/default/files/atoms/files/a_sustained_lunar_presence_nspc_report4220final.pdf
- National Research Council 2007, The Scientific Context for Exploration of the Moon, Final Report (Washington, DC: The National Academies Press)
- Öhmann, T., & Kring, D. A. 2012, *JGRE*, **117**, E00H08
- Paige, D. A., Siegler, M. A., Zhang, J. A., et al. 2010, *Sci*, **330**, 479
- Pieters, C., Head, J., Kring, D., Canup, R., & Scott, D. R. 2018, *COSPAR*, **42**, B3.1-12-18
- Pieters, C. M., Head, J. W., III, Gaddis, L., Jolliff, B., & Duke, M. 2001, *JGR*, **106**, 28001
- Pieters, C. M., Tompkins, S., Head, J. W., & Hess, P. C. 1997, *GeoRL*, **24**, 1903
- Robinson, M. S., Brylow, S. M., Tschimmel, M., et al. 2010, *SSRv*, **150**, 81
- Rubanenko, L., Venkatraman, J., & Paige, D. A. 2019, *NatGe*, **12**, 597
- Saiki, K., Ohtake, M., Nakauchi, Y., et al. 2021, *LPSC*, **51**, 2303
- Sargeant, H. M., Bickel, V. T., Honniball, C. I., et al. 2020, *JGRE*, **125**, e06157
- Sefton-Nash, E., Fissackerly, R., & Trautner, R. 2020, in European Lunar Symp. 2020 Virtual
- Siegler, M., Miller, R., Keane, J., et al. 2016, *Natur*, **531**, 480
- Smith, D. E., Zuber, M. T., Neumann, G. A., et al. 2010, *GeoRL*, **37**, L18204
- Spudis, P. D., Bussey, B., Plescia, J., Josset, J.-L., & Beauvivre, S. 2008, *GeoRL*, **35**, L14201
- Swann, G. A., Bailey, N. G., Batson, R. M., et al. 1977, Geology of the Apollo 14 Landing Site in the Fra Mauro Highlands, Professional Paper 880, USGS, doi:10.3133/pp880
- Thompson, T. W., Masursky, H., Shorthill, R. W., Tyler, G. L., & Zisk, S. H. 1974, *Moon*, **10**, 87
- Torson, J. M. 1989, in VVS '89: Proc. of the 1989 Chapel Hill workshop on Volume Visualization, 33
- Tye, A. R., Fassett, C. I., Head, J. W., et al. 2015, *Icar*, **255**, 70
- Vaughan, W. M., & Head, J. W. 2014, *P&SS*, **91**, 101
- Verrall, R. A., & O'Connell, R. J. 1979, *LPSC*, **10**, 1265
- Warren, P. H., & Rubin, A. E. 2020, *Icar*, **347**, 113771
- Watkins, R. N., Jolliff, B. L., Mistick, K., et al. 2019, *JGRE*, **124**, 2754
- Xiao, Z., Zeng, Z., Ding, N., & Molaro, J. 2013, *E&PSL*, **376**, 1
- Yamamoto, S., Nakamura, R., Matsunaga, T., et al. 2012, *GeoRL*, **39**, L13201
- Zhaoyu, P., Qiong, W., & Yaosi, T. 2015, *Journal of Deep Space Exploration*, **2**, 99
- Zuber, M., Head, J., Smith, D., et al. 2012, *Natur*, **486**, 378